Electrocatalytic performance and cell voltage characteristics of 1st-row transition metal phosphate (TM-Pi) catalysts at neutral pH

Givirovskiy Georgy, Ruuskanen Vesa, Väkiparta Toni, Ahola Jero

Electrocatalytic performance and cell voltage characteristics of 1st-row transition metal phosphate (TM-Pi) catalysts at neutral pH

Georgy Givirovskiy[a], Vesa Ruuskanen[a], Toni Väkiparta[a], Jero Ahola[a]

[a]*LUT University, P.O. Box 20, FI-53851, Lappeenranta, Finland*

Abstract

Water electrolysis represents a clean and sustainable route for large-scale hydrogen generation. However, efficient water splitting is hindered by the kinetically sluggish oxygen evolution reaction (OER), which requires significant energy inputs to drive the reaction at sufficiently fast rates. Recently, an increasing number of applications have emerged that require water electrolysis at neutral pH and under ambient conditions. This requirement creates additional challenges as the electrolysis of water is favorable in acidic and alkaline conditions. In order to tackle these challenges, considerable efforts have been devoted to the development of earth-abundant, highly effective, and robust electrocatalysts for the OER at pH=7. Of these catalysts, amorphous transition-metal phosphates have attracted wide attention because of their unique electrocatalytic properties. In this paper, the OER performance of a series of amorphous first-row transition metal phosphate (TM-Pi) catalysts, namely $Co-Pi$, $NiFe-Pi$ and $Fe-Pi$ prepared with different deposition strategies onto various substrates, is comparatively studied in a neutral phosphate buffer solution (PBS). Additionally, a simplified cell model is applied to analyze the current-voltage characteristics and quantitatively evaluate and compare the reversible, ohmic, and activation overvoltage components of the studied TM-Pi. It is found that TM-Pi catalysts deposited onto a highly ordered nickel foam (NF) substrate are competitive with commercial Pt and IrO_2 catalysts in terms of OER activity and long-term stability.

Keywords: In situ water electrolysis, electrocatalyst, transition metal phosphate, oxygen evolution reaction, pH-neutral electrolyte

1. Introduction

The intensive use of fossil and nuclear energy has exacted a considerable toll on the natural environment and has led to rapid depletion of many natural resources, adverse climate impacts from greenhouse gas emissions, as well as water, air and land pollution. Growing public awareness of climate change and other environmental issues have resulted in demands for clean and sustainable technologies based on renewable energy [1, 2, 3]. Hydrogen, which is the simplest and lightest element of the periodic table, has a high energy density and is considered an eco-friendly fuel to meet the world's increasing energy demand. Currently, the major part of hydrogen production is based on fossil fuel refining processes, such as steam reforming or partial oxidation of methane, which release significant amounts of carbon dioxide into the atmosphere. In contrast, electrochemical water splitting based on renewable electricity provides a sustainable carbon-neutral route for storing energy from intermittent sources using hydrogen as a carrier [4, 5].

The water electrolysis process has formed the basis for a number of different energy storage or conversion devices, of which the most efficient and robust are electrolyzers [6, 7], fuel cells [8], and metal-air batteries [9]. Bio-electrochemical systems (BES) [10] and hybrid biological-inorganic (HBI) systems [11] represent a fast-developing area of research and are interesting examples of integrating water electrolysis into the biological process to fix carbon dioxide into multicarbon organic compounds. Even though the module design of such systems varies, a common factor is that they are all two-electrode systems involving the hydrogen evolution reaction (HER) or oxygen reduction reaction (ORR) at the cathode and water oxidation or the oxygen evolution reaction (OER) at the anode [12]. The common constraint of these systems is the sluggish kinetics of the oxygen evolution reaction (OER) in which molecular oxygen is formed through a complex pathway involving the extraction of four electrons and four protons. The hydrogen evolution reaction (HER) however is exclusively a two-electron transfer reaction and, therefore, requires substantially less energy (overpotential) to overcome the kinetics of the reaction [12, 13].

The oxygen evolution reaction (OER) is highly pH-dependent. In alkaline conditions, four hydroxyl groups (OH^-) are oxidized into two water molecules (H_2O) and one molecule of oxygen (O_2), while in acidic and neutral conditions, two water molecules (H_2O) are oxidized to be transformed into four protons (H^+) and one oxygen molecule (O_2) [13]. Electrochemical water split-

ting is hindered by the high stability of water, which requires $237 \, \mathrm{kJ \, mol^{-1}}$ of Gibbs free energy change for the overall reaction [14]. According to the thermodynamics, the equilibrium or reversible cell voltage, which is the lowest potential required for the electrolysis to take place at 25 °C and 1 atm, is equal to 1.23 V. In practice, however, commercial electrolyzers typically operate in the range of 1.8–2.1 V, indicating that water electrolysis proceeds far from its equilibrium potential [15]. Significant energy losses caused by the large overpotentials required to drive water splitting at sufficiently fast rates are mainly the result of the kinetically sluggish oxygen evolution reaction (OER) [12, 13, 16]. Therefore, highly efficient OER catalysts are required to lower the energy barrier and increase the overall efficiency of the water splitting process.

At the present time, noble metal-based catalysts made of ruthenium (Ru) and iridium (Ir) and especially their oxides exhibit superior performance for OER and are considered benchmark catalysts. A major drawback of these materials is their unsuitability for large-scale applications owing to their high cost and scarcity. In addition, in both acidic and alkaline electrolytes, IrO_2 and RuO_2 experience stability issues at high anodic potentials because of their oxidation into IrO_3 and RuO_4, respectively, and further dissolution in the electrolyte [12]. Considerable efforts have been therefore made to develop active, stable and low-cost catalysts made of earth-abundant materials capable of operating at low overpotentials at different pHs as substitutes for precious metal catalysts [12, 13].

Various transition metal (TM) oxides [17, 18, 19], hydroxides [20], sulfides [21, 22], nitrides [23, 24], borides [25, 26], carbides [27, 28], selenides [29] and phosphides [30, 23, 31, 32, 33] have been extensively investigated as efficient catalysts for overall water splitting. Transition metal phosphates (TM-Pi) have attracted widespread scientific interest after the development of a cobalt phosphate (Co−Pi) catalyst by Matthew W. Kanan and Daniel G. Nocera in 2008 [34]. In subsequent studies, numerous other TM-Pi catalysts have been developed, and their electrocatalytic activity towards OER and HER has been shown. A common feature of all these catalysts is the doping of phosphate groups into a crystal lattice of transition metals, such as Ir [16, 35], Fe [36, 37], Co [34, 35], Ni [38, 39, 40, 41] and Mn [42] by different methods including electrodeposition, precipitation and hydrothermal synthesis. Phosphate groups facilitate the oxidation of metal atoms during the proton-coupled electron transfer process and distort the native atomic geometry favoring adsorption and oxidation of water molecules [43]. As a

3

result of this unique feature, several reported catalysts, such as $Ir-Pi$ and $IrCo-Pi$, exhibit an intrinsic performance superior to the benchmark IrO_2 [16, 35]. However, even though the content of Ir in $IrCo-Pi$ has been reduced by 50%, there is still a considerable capacity for optimization and reduction in expensive Ir usage.

In the present paper, a series of first-row transition metal phosphates (TM-Pi) are prepared and tested in a neutral phosphate buffer solution (PBS). It is well known that water electrolysis is kinetically difficult in pH-neutral conditions and more favorable in basic and acidic conditions because of the deprotonated molecules available for oxygen and hydrogen evolution reactions [14]. However, pH-neutral conditions exert a significantly less corrosive effect on the electrochemical devices and are vital for emerging biological processes with integrated water electrolysis. The materials analyzed included $Co-Pi$, $Fe-Pi$ and $NiFe-Pi$. $Co-Pi$ was selected as a benchmark catalyst from the TM-Pi family, which was exclusively developed to perform water splitting in artificial photosynthesis systems at neutral pH under ambient conditions [34]. Iron (Fe) is the cheapest and most abundant TM in the Earth's crust. Therefore, $Fe-Pi$ prepared by a simple and cheap successive ionic layer deposition and reaction (SILAR) method [36, 37] was selected as a candidate for analysis. Literature review suggests that $Ni-Fe$ catalysts provide a promising alternative to catalysts based on precious metals. It is noteworthy that $Ni-Fe$ catalysts are considerably more active for OER than pure Ni or Fe [39, 41]. Consequently, bimetallic $NiFe-Pi$ [39] was selected to quantify the synergistic effect of iron in NiFe-based structures. The performance of $Fe-Pi$ and $NiFe-Pi$ has been extensively studied in an alkaline medium, but to the authors' knowledge, it has not been studied in detail in neutral conditions. The main contribution of the present study is the comparative analysis of TM-Pi catalyst on different substrates under neutral conditions. A simplified mathematical electrolyzer cell model is used to deconvolute different overpotentials based on measured current–voltage characteristics.

2. Experimental section

2.1. Materials

Analytical grade reagents $NiSO_4 \cdot 6\,H_2O$, $FeSO_4 \cdot 7\,H_2O$, NaH_2PO_2, $NaOAc \cdot 3\,H_2O$, KH_2PO_4, K_2HPO_4, $Co(NO_3)_2 \cdot 6\,H_2O$, $FeCl_3 \cdot 6\,H_2O$, ethanol, and acetone

4

were purchased from Sigma-Aldrich, USA. All chemicals were used as received without additional purification. Graphite electrodes were acquired from Gamry Instruments, USA. Titanium (Ti) coated with IrO_2, and Pt catalysts were purchased from PV3 Technologies, UK. Nickel foam (NF, thickness: 2mm, porosity: 97%, purity: 99.8%, PPI: 110) was acquired from Tmax Battery Equipments Limited Company, China.

2.2. Catalyst fabrication (NiFe–Pi, Co–Pi, and Fe–Pi)

The procedure for catalyst fabrication was adopted from previous reports [34, 37, 39]. Electrodeposition and successive ionic layer deposition and reaction (SILAR) were the methods used for catalyst fabrication. The electrodeposition was carried out in the experimental setup depicted in Fig. 1. The setup consisted of: (i) a three-electrode electrolyzer cell with a cross-sectional area of $2.6\,cm^2$; (ii) a WaveNow potentiostat to conduct electrochemical measurements; (iii) a constant flow pump to circulate the electrolyte through the external vessel equipped with the temperature measurement; and (iv) a water bath with an immersed Lauda heater to maintain constant temperature.
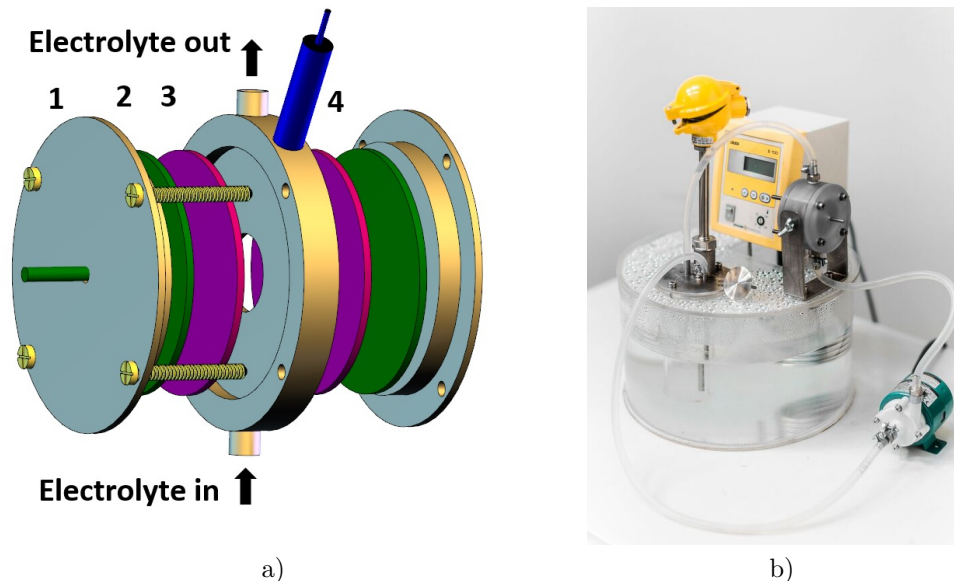

Fig. 1. Experimental setup used for the electrolysis tests. (a) 3D model of the electrolyzer cell; 1: teflon frame, 2: conductive stainless steel plates, 3: working and counter electrodes, 4: reference electrode (Ag/AgCl). (b) Photo of the experimental setup.

Graphite and nickel foam (NF) were used as substrates for deposition of the catalysts. Prior to deposition, a circular piece of NF ($15.2\,\mathrm{cm}^2$) was cleaned in 2M HCL to remove the nickel oxide layer. Subsequently, ultrasonic cleaning was performed in ethanol, acetone and distilled deionized water to complete removal of surface contaminants. Pretreatment of the graphite substrates included polishing with sandpaper and rinsing with acetone and distilled deionized water. All samples were dried in ambient air prior to the deposition of the TM-Pi catalysts.

The NiFe−Pi catalyst was prepared with a cathodic electrodeposition strategy by cyclic voltammetry (CV) in the potential range from -1.2 to - 0.7 V (vs.Ag/AgCl) at a scan rate of 5 mV/s for 8 cycles. The aqueous source solution contained 0.0125, 0.025, 0.0375 M $NiSO_4 \cdot 6\,H_2O$, 0.0125, 0.025, 0.0375 M $FeSO_4 \cdot 7\,H_2O$, 0.5 M NaH_2PO_2, and 0.1 M $NaOAc \cdot 3\,H_2O$ dissolved in distilled deionized water. The Co−Pi catalyst was prepared with an anodic electrodeposition strategy by CV at a scan rate of 5 mV/s for 100 cycles. Potential ranges from 0.9 to 1.2 V (vs.Ag/AgCl) and from 0.8 to 1.1 V (vs.Ag/AgCl) were used when depositing onto graphite and NF, respectively. To obtain the solution for the electrodeposition, 0.5 mM of $Co(NO_3)_2 \cdot 6\,H_2O$ was added to the phosphate buffer solution (PBS), which was prepared by mixing 0.1 M KH_2PO_4 and 0.1 M K_2HPO_4. In both electrodeposition methods, graphite and NF were used as the working electrodes (WE), while a stainless steel plate was used as the counter electrode (CE). For the SILAR deposition method, 10 mM aqueous solutions of KH_2PO_4 and $FeCl_3 \cdot 6\,H_2O$ were prepared separately as the sources of cations and anions, respectively. To prepare the Fe−Pi coating, the cleaned substrates were successively immersed first in a KH_2PO_4 solution for 10 s and then immediately in a $FeCl_3 \cdot 6\,H_2O$ solution for 10 s. This procedure was repeated for 10 min. All solutions were prepared in ultrapure doubly distilled water obtained from a PURELAB flex system. After deposition, all samples were again gently rinsed with distilled deionized water and dried in ambient air before the elctrochemical measurement tests.

2.3. Material characterization

A Hitachi S-3400N field-emission scanning electron microscope (SEM) equipped with energy dispersive X-ray spectroscopy (EDX) measurement was used to examine the surface morphologies and the compositional distribution of the elements of the fabricated catalysts. SEM images were obtained by

operating the microscope at 10 kV and 20 mA using a UDV (secondary electron detector) and a BSE (backscatter electron detector). X-ray diffraction (XRD) analysis performed with a Bruker D8 Advance X-ray diffractometer was used to analyze the crystal structure of the studied TM-Pi catalysts. XRD patterns were obtained at 40 kV, 30 mA with Cu Kα-type radiation.

2.4. Electrochemical measurements

All the electrochemical measurements were conducted with a WaveNow Potentiostat from Pine Research Instrumentation, USA, in the three-electrode system shown in Fig. 1. As-prepared TM-Pi catalysts deposited on NF or graphite were directly used as the working electrodes (WE) without further treatment. A titanium (Ti) coated with a Pt circular electrode plate and an Ag/AgCl,Cl$^-$ (3M) electrode were used as the counter electrode (CE) and the reference electrode (RE), respectively. Polarization curves were obtained by linear sweep voltammetry (LSV) at a scan rate of $5\,\mathrm{mV\,s^{-1}}$ in a PBS solution, which was prepared by mixing 0.1 M KH$_2$PO$_4$ and 0.1 M K$_2$HPO$_4$. Long-term durability tests were carried out in the chronopotentiometry mode for 36 h in a PBS. All the potentials measured in this work were calibrated to a reversible hydrogen electrode (RHE) using the following equation:

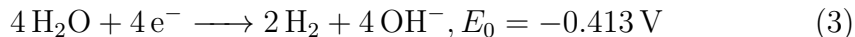$$E_{\mathrm{RHE}} = E_{\mathrm{Ag/AgCl}} + 0.1976\,\mathrm{V} + 0.059\,\mathrm{pH} \tag{1}$$

2.5. Cell model

Water electrolysis in neutral conditions (pH=7) is described by the following electrochemical reactions [14].

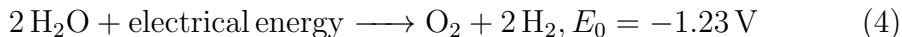The oxidation half-reaction at the anode–oxygen evolution reaction (OER):

$$2\,\mathrm{H_2O} \longrightarrow \mathrm{O_2} + 4\,\mathrm{H^+} + 4\,\mathrm{e^-}, E_0 = 0.817\,\mathrm{V} \tag{2}$$
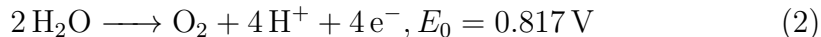
The reduction half-reaction at the cathode–hydrogen evolution reaction (HER):

$$4\,\mathrm{H_2O} + 4\,\mathrm{e^-} \longrightarrow 2\,\mathrm{H_2} + 4\,\mathrm{OH^-}, E_0 = -0.413\,\mathrm{V} \tag{3}$$

The overall reaction in the electrolytic cell:

$$2\,\mathrm{H_2O} + \mathrm{electrical\,energy} \longrightarrow \mathrm{O_2} + 2\,\mathrm{H_2}, E_0 = -1.23\,\mathrm{V} \tag{4}$$

Virtually, higher voltages than equilibrium or reversible voltage (1.23 V) are required to initiate the dissociation of water. The high overvoltage and

the subsequent energy loss are mainly caused by the additional overvoltages presented in the following equation [15]:

$$U_{\text{cell}} = U_{\text{rev}} + U_{\text{ohm}} + U_{\text{act}} + U_{\text{con}}, \tag{5}$$

where U_{cell} is the cell voltage, U_{rev} is the reversible open circuit voltage, U_{ohm} is the overvoltage caused by ohmic losses in the cell elements, U_{act} is the activation overvoltage caused by electrode kinetics, and U_{con} is the concentration overvoltage caused by mass transport processes (usually, U_{con} is much lower than U_{ohm} and U_{act}, and it can thus be neglected).

A water electrolysis model developed and validated in our previous studies [44, 45] was applied to analyze the collected current–voltage characteristics. The simplified cell model presented in the equation below allows quantitative evaluation and comparison of reversible, ohmic (the 2nd term in the equation after the equal sign) and activation overvoltages (the 3rd term in the equation after the equal sign) of different electrode sets.

$$U_{\text{cell}} = U_{\text{rev}} + \frac{\delta_{\text{m}} i_{\text{cell}}}{\sigma_{\text{m}}} + \alpha \operatorname{arcsinh}\left(\frac{i_{\text{cell}}}{2i_0}\right), \tag{6}$$

where δ_{m} is the distance between the electrodes (expressed in cm), i_{cell} is the current density (A cm^{-2}), σ_{m} is the conductivity of the electrolyte (S cm^{-1}), α is the charge transfer coefficient, and i_{o} is the exchange current density on the electrode surfaces. U_{rev}, σ_{m}, α, and i_0 are the parameters to be fitted by the experimental data.

3. Results and discussion

3.1. TM-Pi catalyst formation

Typical CV curves of the NiFe–Pi and Co–Pi electrodeposition process are presented in Fig. 2. The CV approach ensures fast deposition of TM ions in different potential ranges, and it is beneficial in comparison with traditional potentiostatic deposition of TM-Pi catalysts. It can be clearly seen from the curves that there is a steep increase in the voltammetric current observed over the first 20–30 cycles and a subsequent gradual increase during the electrodeposition of Co–Pi. A similar behavior can be observed in the potential region of the HER; the voltammetric current decreases fast at the beginning of the deposition of NiFe–Pi, and slows down at the end. It would appear that the increasing coverage of the substrate surface and the rising

thickness of the TM-Pi coating accelerate the rate of the electrolysis reaction in both cases. After deposition of NiFe−Pi and Co−Pi, the central part of the NF substrate was evenly coated with a dark coating. When depositing NiFe−Pi onto graphite, the surface coating had a silver color as seen in Fig. 3.
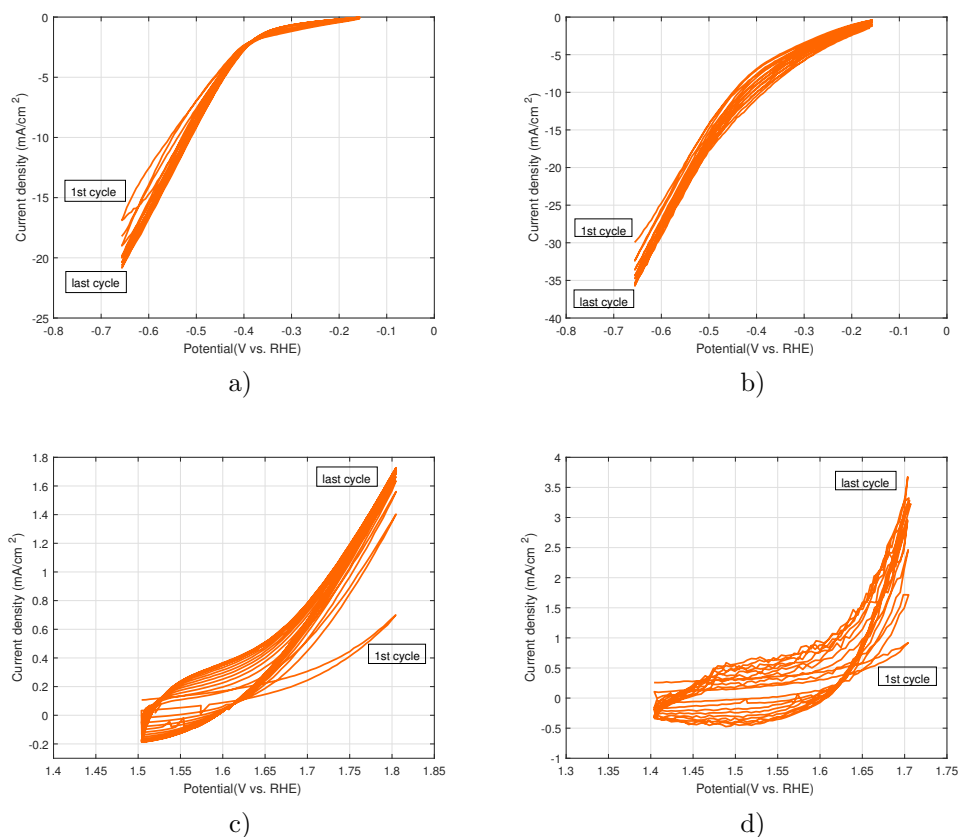

Fig. 2. Cyclic voltammograms of the deposition process of (a) NiFe-Pi onto graphite, (b) NiFe-Pi onto NF, (c) Co-Pi onto graphite and (d) Co-Pi onto NF.

The SILAR deposition method to prepare Fe−Pi is considered an inexpensive and facile strategy. Successive immersion of the substrate in the 10 mM cation solution of KH_2PO_4 and the 10 mM anion solution of $FeCl_3 \cdot 6\,H_2O$ for 10 min resulted in the formation of a white flocculent precipitate all over the surface which could be easily detected with the naked eye.
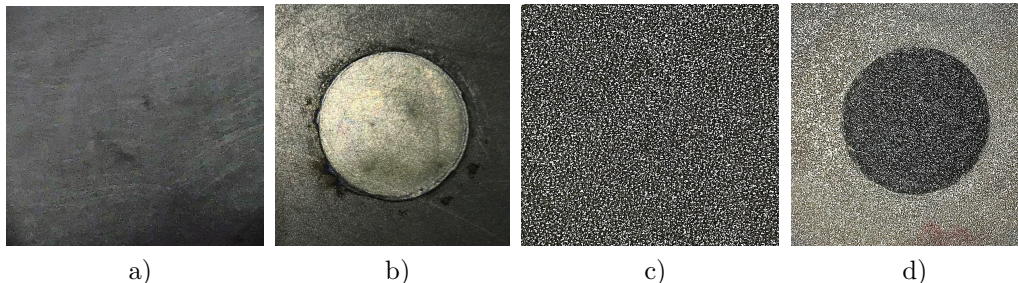
Fig. 3. Photos of electrode surfaces: (a) bare graphite, (b) graphite coated with NiFe-Pi, (c) NF, and (d) NF coated with Co-Pi.

3.2. Physical characterization

XRD patterns were recorded for the substrate prior to and after the catalyst deposition. A typical XRD diagram of the TM-Pi catalysts deposited on NF is presented in Fig. 4. Diffraction peaks were observed at 44.5°, 55.8°, and 76.4° for the NF substrate. The peaks indicates that all the synthesized TM-Pi catalysts are amorphous in nature.
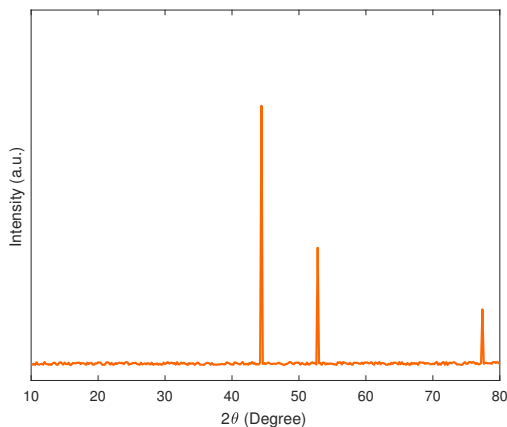

Fig. 4. Typical XRD diagram of the TM-Pi catalysts deposited on NF.

The morphology of the TM-Pi catalysts was studied using SEM. Fig. 5 shows SEM images of bare NF and as-deposited Fe-Pi and Co-Pi, while Fig. 6 depicts the surface morphology and elemental mapping of NiFe-Pi deposited on the NF substrate. The SEM analysis revealed that the surface of the NF was completely and uniformly coated with TM-Pi catalysts in all cases. The

10

example of elemental mapping in Fig. 6d shows uniform distribution of Ni, Fe, and P in the film of NiFe-Pi catalysts. This observation applied also to other TM-Pi catalysts. According to SEM images at high magnification, all TM-Pi catalysts have different surface structures. In particular, the Fe-Pi coating demonstrates a highly rippled flake structure with numerous agglomerates. A Co-Pi layer is formed on the surface of the NF substrate with numerous 3D-porous micrometer-size particles on top of the film. Hierarchical NiFe-Pi mainly consists of nanobubbles with sizes ranging from approximately 200 nm to 500 nm. Cracks observed in all the TM-Pi catalysts at higher magnifications probably result from loss of water when drying of samples in ambient air.

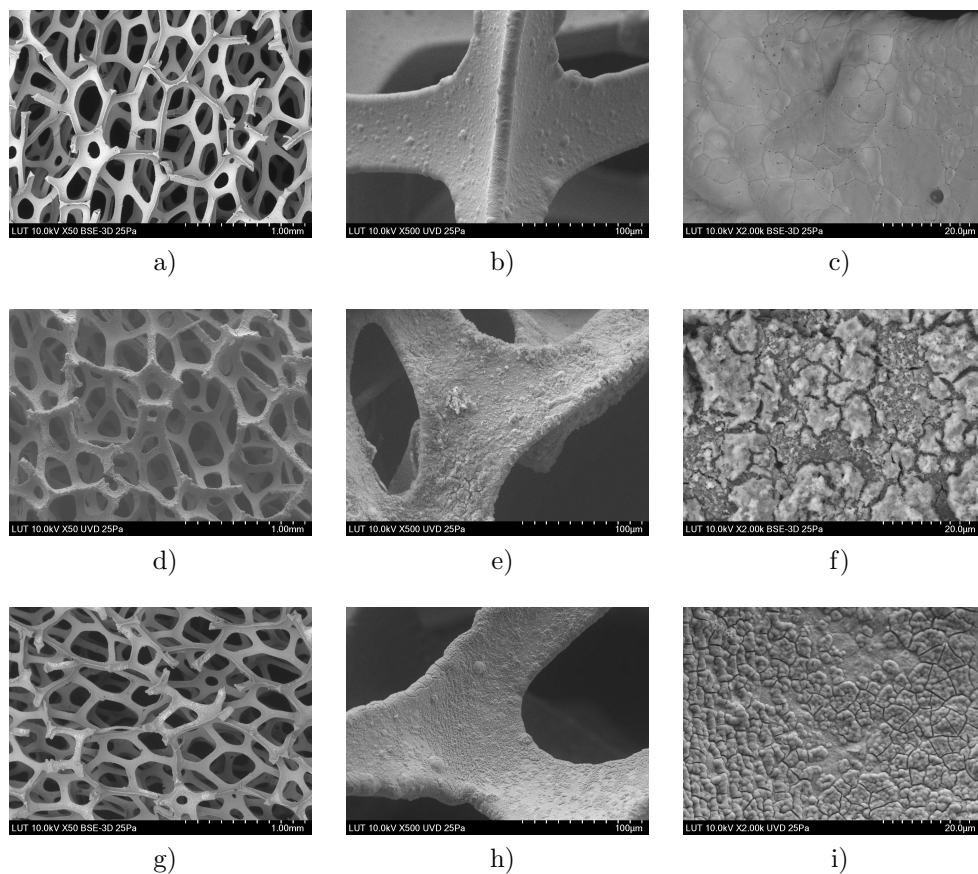**Fig. 5.** SEM images of (a–c) bare nickel foam (NF), (d–f) Fe-Pi on NF and (g–i) Co-Pi on NF at different magnifications.
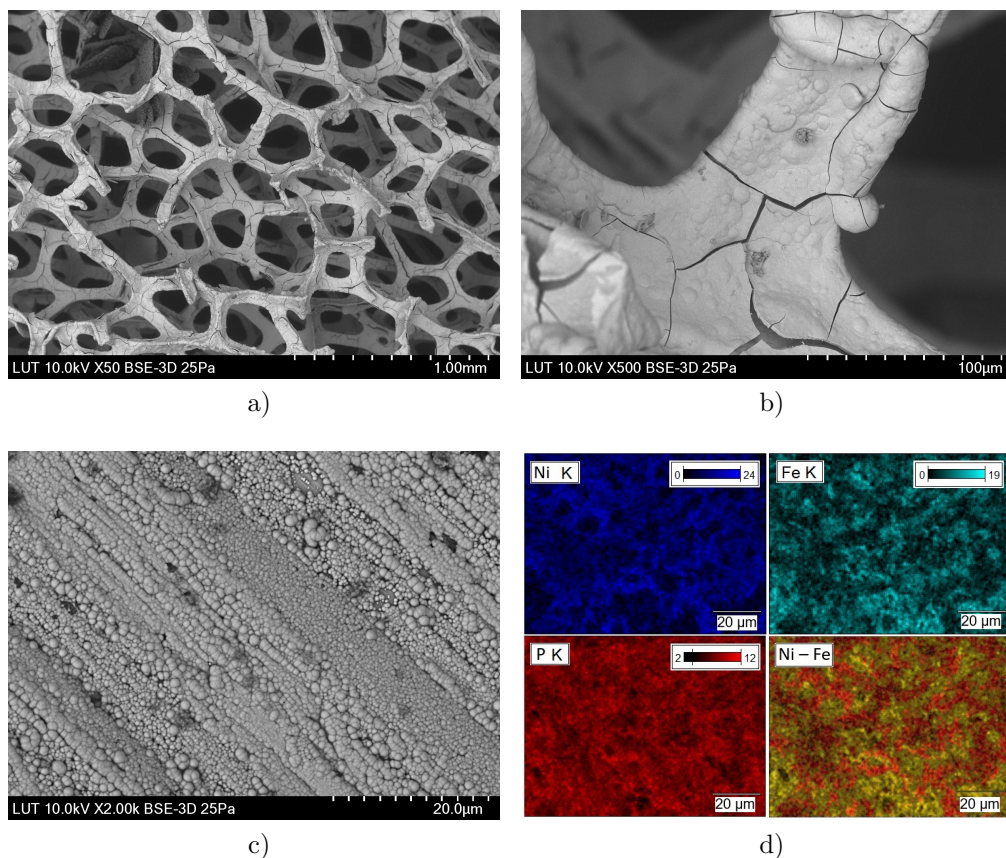
11

Fig. 6. SEM images of (a–c) NiFe-Pi on NF at different magnifications and (d) the corresponding EDS elemental mappings.

The EDXA spectra of bare NF and TM-Pi catalysts are depicted in Fig. 7. The presence of Ni, Fe, Co, and P can be verified from the corresponding peaks in the EDXA diagrams. The quantitative EDXA analysis showed that for Co-Pi catalyst a Co:P ratio varied from 2.5-3:1, while for Fe-Pi a typical Fe:P indicated a ratio of 1:2.2-2.5. The NiFe-Pi catalysts were prepared with different Ni/Fe wt.% compositions. The EDXA showed that the weight percent of Ni and Fe in the NiFe-Pi catalyst deposited onto graphite was close to the theoretical composition in all cases. For instance, for NiFe-Pi catalyst a Ni:Fe:P ratio was approximately 8:1:1.6. The amount of Ni was much higher when using the NF substrate, which can be explained by the EDXA spectrum probe, which reaches the NF substrate due to penetration
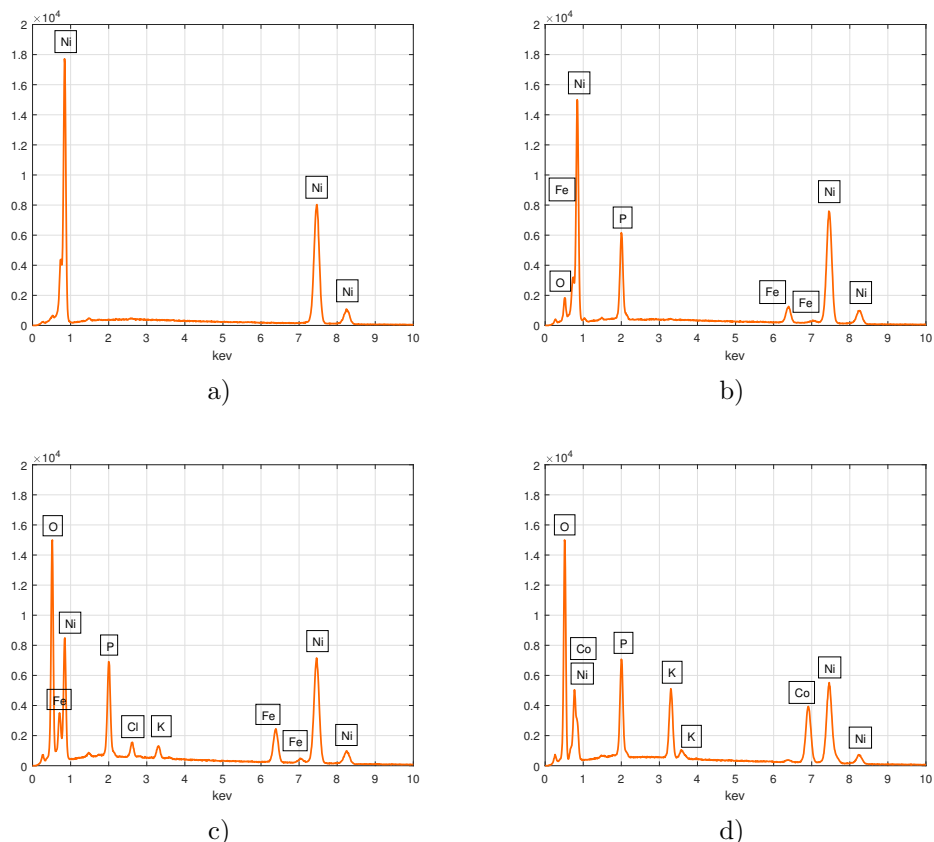
12

²⁵⁸ through the thin catalyst layer.

Fig. 7. EDXA spectra for (a) bare nickel foam (NF), (b) NiFe-Pi on NF and (d) Co-Pi on NF.

²⁵⁹ *3.3. Catalytic activity*

²⁶⁰ The electrochemical activity of all TM-Pi catalysts was evaluated using
²⁶¹ a three-electrode electrolyzer prototype in a neutral PBS electrolyte. In
²⁶² order to find the optimal Ni/Fe composition, NiFe-Pi catalyst deposited onto
²⁶³ the graphite substrate with different compositional ratios of Ni and Fe were
²⁶⁴ compared with each other. It was found that electrodes with 25 wt.% of
²⁶⁵ Ni and 75 wt.% of Fe showed the worst electrochemical activity and the
²⁶⁶ highest overpotential. Electrodes with a 50/50 wt.% composition of Ni/Fe

13

had a slightly better OER performance than electrodes with 75/25 wt.%, and thus, the optimal 50/50 wt.% composition was used in subsequent tests.

One objective of the study was to investigate the role of the substrate material in the performance of TM-Pi catalysts. In the present study, graphite was selected as a flat, cheap, and commonly used electrode material, while NF was selected as a substrate with a high specific surface area and good OER activity. Figs. 8a and b show the polarization curves of all TM-Pi catalysts deposited onto graphite and NF at a scan rate of $5\,\mathrm{mV\,s^{-1}}$ in a neutral PBS. The performance of the TM-Pi electrodes was compared with commercial noble materials, represented by Pt and IrO_2. It can be clearly seen that even though the composition of the catalyst layer is the most important parameter determining the OER activity, the nature of the substrate onto which the catalyst is deposited also plays a significant role. When studying TM-Pi catalysts deposited onto graphite, the LSV curves revealed that there was no current flow until the potential reached $1.5\,\mathrm{V}$ for all the studied electrodes. After $1.5\,\mathrm{V}$, the current at noble Pt and IrO_2 started to rise steeply reaching a current density of $1\,\mathrm{mA\,cm^{-2}}$ at overpotentials of $450\,\mathrm{mV}$ and $430\,\mathrm{mV}$, respectively. In the case of $Co-Pi$ deposited onto graphite, after $1.5\,\mathrm{V}$, the current increase was less steep, reaching $1\,\mathrm{mA\,cm^{-2}}$ at a significantly higher overpotential of $510\,\mathrm{mV}$. The $Fe-Pi$ and $NiFe-Pi$ catalysts deposited onto graphite were approximately similar in performance, having the onset potential at $1.6\,\mathrm{V}$ and reaching current densities of $0.6\,\mathrm{mA\,cm^{-2}}$ and $0.88\,\mathrm{mA\,cm^{-2}}$ at $1.8\,\mathrm{V}$, respectively.

The electrocatalytic OER activity of the series of TM-Pi was considerably enhanced when deposited onto the NF substrate. As shown in Fig. 8b, all the TM-Pi catalysts exhibited an onset overpotential comparable with the commercial Pt and IrO_2 electrodes. The reference current density of $1\,\mathrm{mA\,cm^{-2}}$ was reached at overpotentials of $420\,\mathrm{mV}$, $495\,\mathrm{mV}$, and $534\,\mathrm{mV}$ for Co-Pi, NiFe-Pi, and Fe-Pi, respectively. Notably, the OER performance of the Co-Pi catalyst deposited onto the NF surpassed that of the noble electrodes during the whole water splitting process. The superior OER activity of Co-Pi is due to both the high active surface area and the high intrinsic catalytic effect. NiFe-Pi and Fe-Pi were once again similar in performance; however, when the potential reached 1.7 V, the activity of NiFe-Pi increased significantly, and the current density reached $4.45\,\mathrm{mA\,cm^{-2}}$ at 1.8 V, exceeding that of the Pt and IrO_2 electrodes. The current density of Fe-Pi/NF was about 2.8 times as low as that of NiFe-Pi/NF and almost 3.4 times as low as that of Co-Pi/NF at the end of the electrolysis process.
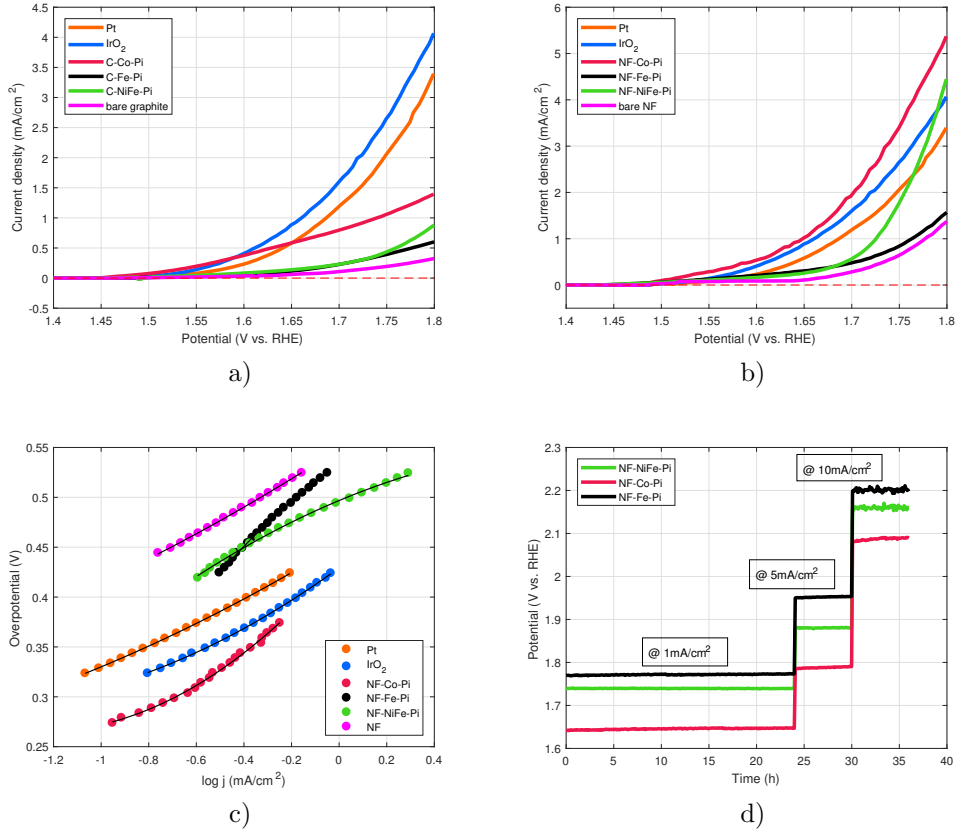
14

Fig. 8. OER catalytic properties of different catalysts in a PBS with pH=7: (a) LSV curves of TM-Pi deposited onto graphite vs. noble catalysts, (b) LSV curves of TM-Pi deposited onto NF vs. noble catalysts, (c) corresponding Tafel plots and (d) long-term stability tests of TM-Pi.

In general, the performance of the TM-Pi-containing electrodes is far better than that of the bare substrates, especially for the NF series. Although the coating on all the studied electrodes has the same geometric surface area of $2.6\,\mathrm{cm}^2$, the real active area of the catalyst layer is much higher on the NF substrate because of its unique morphology (Figs. 5a–c). The greater active area explains the high electrocatalytic activity once the TM-Pi electrocatalysts are loaded on the NF. In light of the higher electrocatalytic activity, the TM-Pi catalysts prepared on NF were selected for further characterization and evaluation of the OER performance in the present study.

15

The Tafel slope is an essential representative parameter for evaluation of OER kinetics. Tafel slopes of TM-Pi/NF were determined from the data shown in Fig. 8c. Analysis revealed that IrO_2 and Co-Pi exhibited almost similar Tafel slopes of approximately 60 mV/dec. This value is representative for a chemical rate-determining step in which a fast OER occurs with the OH surface species rearrangement through a surface reaction [46]. Other tested catalysts showed exceptionally high Tafel slopes close to or higher than 120 mV/dec, which is consistent with the comparatively slow OER kinetics characterized by adsorption and discharge of OH- ions as a chemical rate-determining step. Detailed description of kinetic equations under different reaction conditions can be found in [47] while the mechanistic schemes are well-presented in [12]. In general, the mechanism for OER in neutral and alkaline conditions can be described by the following equations [16]:

$$S + OH^- \rightleftharpoons S-OH + e^- \tag{7}$$

$$S-OH + OH^- \rightleftharpoons S-O + H_2O + e^- \tag{8}$$

$$2\,S-O \rightleftharpoons 2\,S + O_2 \tag{9}$$

where S represents active sites on the catalyst while S–OH and S–O stand for adsorbed intermediates.

When the Tafel slope is close to 120 mV/dec, reaction described by equation 7 represents a rate-determining step. However, the rate-determining step for Tafel slope of 60 mV/dec is different. It is considered that reaction described by equation 7 is divided into the following steps and step described by equation 11 is the rate-determining step for 60 mV/dec:

$$S + OH^- \rightleftharpoons S-OH^* + e^- \tag{10}$$
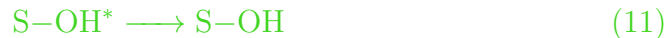
$$S-OH^* \longrightarrow S-OH \tag{11}$$

where S–OH* and S–OH stand for adsorbed intermediates with the same chemical structure, but different energy states.

Stability is an important parameter in evaluation of catalyst performance in practical applications. In this study, stability measurements for a series of
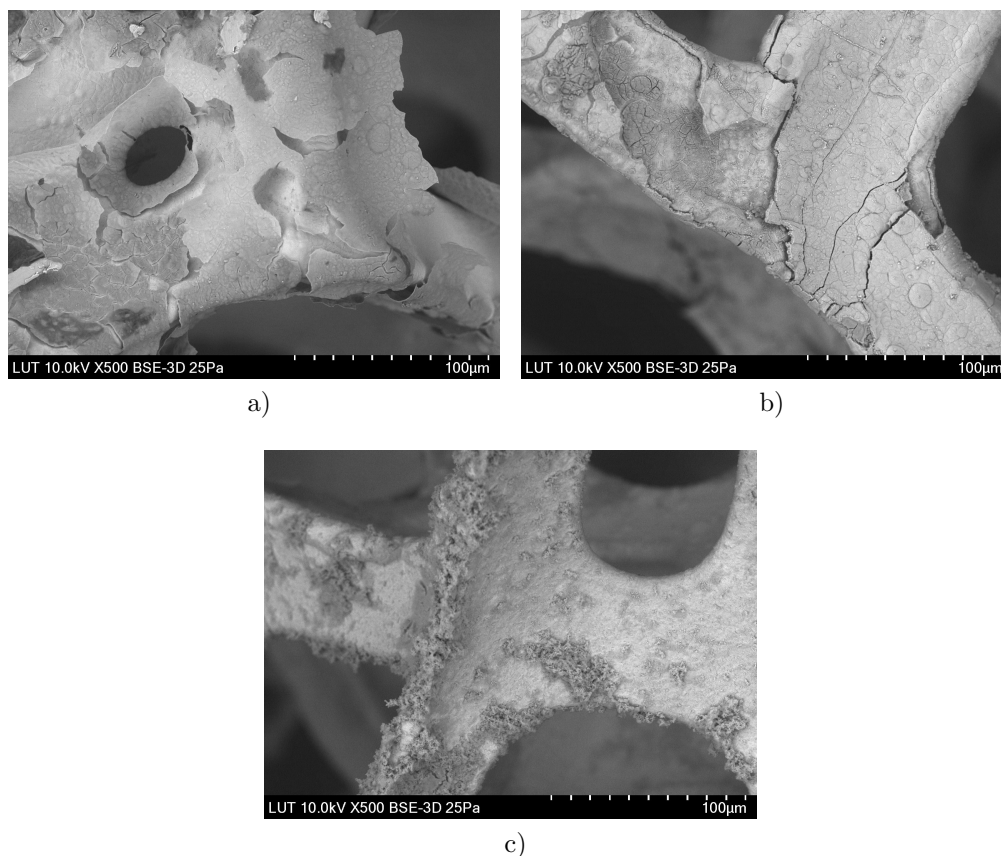
16

Fig. 9. SEM images recovered after the long-term durability tests for (a) Co-Pi/NF, (b) NiFe-Pi/NF and (c) Fe-Pi/NF.

TM-Pi/NF were performed successively at a constant current density of 1, 5, and $10\,\mathrm{mA\,cm^{-2}}$ for 36 h in the PBS solution (Fig. 8d). Fig. 9 shows SEM images of TM-Pi/NF after the 36 h durability test. It can be seen that the catalyst layer is partly detached from the substrate surface. Nevertheless, the catalysts continued to maintain a stable potential during the operation of water splitting. The stable operation indicates that an essential part of the TM-Pi catalysts remains on the surface, and its amount is sufficient to maintain the same level of activity. The formation of bubbles on the electrode surfaces under vigorous oxygen evolution and partial loss of effective catalyst may explain the minor increase in the overpotential over time for all the studied catalyst materials.

17

3.4. Overvoltage analysis

In the present study, a simplified cell model was used to describe the cell voltage components as a function of current density for various TM-Pi deposited onto NF in a pH-neutral PBS. To apply a developed model, the voltage and current were measured with the same electrolyzer prototype but using a two-electrode configuration to measure the whole cell. Cell voltage as a function of current density is presented in Fig. 10a. Again, NF coated with an appropriate TM-Pi catalyst was used as a working electrode, the Pt plate acting as a counter and reference electrode simultaneously. The parameters U_{rev}, σ_{m}, α, and i_0 in Eq. (6) were determined using experimental voltage and current data and the method of nonlinear least square regression, and presented in Table 1. Further, the reversible voltage, the ohmic voltage, and the activation voltage terms are presented separately in Figs. 10b–d.

Table 1. Experimentally fitted parameters of the simplified cell model with various TM-Pi catalysts deposited onto NF as anodes.

Anode material	U_{rev} (V)	σ_{m} (S cm^{-1})	α (-)	i_0 (A cm^{-2})
NF-NiFe-Pi	1.5799	0.0220	0.1801	0.0001
NF-Co-Pi	1.5166	0.0223	0.1708	0.0001
NF-Fe-Pi	1.5627	0.0222	0.2180	0.0001

Table 2. Reversible voltage, ohmic overvoltage, and activation overvoltage at reference current density of $10\,\mathrm{mA\,m^{-2}}$ for various TM-Pi catalysts deposited onto NF.

Anode material	U_{rev} (V)	U_{ohm} (V)	U_{act} (V)	U_{cell} (V)
NF-NiFe-Pi	1.5799	0.2500	0.8294	2.6593
NF-Co-Pi	1.5166	0.2466	0.7866	2.5498
NF-Fe-Pi	1.5627	0.2477	1.0039	2.8143

Fig. 10 shows clearly that the measured data are in good agreement with the experiments with the three-electrode setup. The obtained Co-Pi/NF exhibited the lowest U_{rev} (Table 1) and outperformed NiFe-Pi/NF and Fe-Pi/NF throughout the water splitting process. The ohmic overpotential (σ_{m}), which is mainly caused by the voltage drop across the PBS electrolyte, was
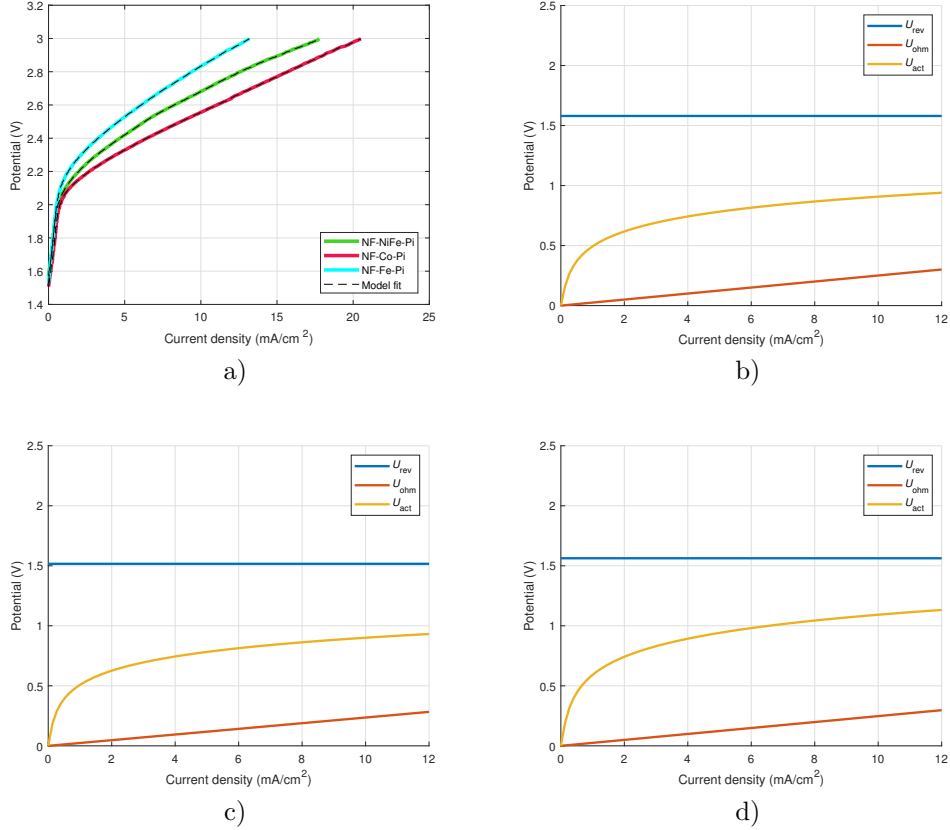
Fig. 10. Overvoltage analysis of the TM-Pi catalysts: (a) cell voltage as a function of current density and the fitted simplified mathematical model; reversible voltage, ohmic overvoltage, and activation overvoltage as a function of current density for (b) NiFe-Pi onto NF, (c) Co-Pi onto NF and (d) Fe-Pi onto NF.

approximately similar for all the tested TM-Pi catalysts. The reversible voltage, ohmic overvoltage, and activation overvoltage at reference current density of $10\,\mathrm{mA\,cm^{-2}}$ for various TM-Pi catalysts deposited onto NF are summarized in Table 2. The obtained values match well with the experimentally measured conductivity of the PBS of $22.5\,\mathrm{mS\,cm^{-1}}$ which supports the use of the simplified cell model.

19

4. Conclusions

A comparative study of the OER activity, stability and overvoltage components of amorphous TM-Pi catalysts deposited by different strategies onto different substrates was presented in this paper. The experimentally observed intrinsic OER activities for the studied catalysts in a neutral PBS decreased in the order of Co-Pi > NiFe-Pi > Fe-Pi. The catalysts exhibited activity comparable with or exceeding that of commercial precious Pt and IrO_2 when deposited onto a substrate with a high specific surface area such as NF. The reference current density of $1\,\mathrm{mA\,cm^{-2}}$ was reached at relatively small overpotentials of $420\,\mathrm{mV}$, $495\,\mathrm{mV}$, and $534\,\mathrm{mV}$ for Co-Pi, NiFe-Pi, and Fe-Pi, respectively. A simplified cell model was used to evaluate the current-voltage characteristics of the studied TM-Pi catalysts and to separate the reversible voltage, the ohmic voltage, and the activation voltage terms. All the studied TM-Pi catalysts exhibited sufficient stability for the OER during the 36 h durability tests in the electrolyzer prototype. The collected data and the proposed simplified cell model are valuable for further studies and evaluation of TM-Pi electrocatalyst performance.

20

References

[1] D. G. Nocera, M. P. Nash, Powering the planet: Chemical challenges in solar energy utilization, PNAS 103 (43) (2006) 15729–15735. doi:https://doi.org/10.1073/pnas.0603395103.

[2] T. W. Brown, T. Bischof-niemz, K. Blok, C. Breyer, H. Lund, B. V. Mathiesen, Response to Burden of proof : A comprehensive review of the feasibility of 100 % renewable-electricity systems ', Renewable and Sustainable Energy Reviews 92 (September 2017) (2018) 834–847. doi:10.1016/j.rser.2018.04.113.
URL https://doi.org/10.1016/j.rser.2018.04.113

[3] F. Vidal, J. Koponen, V. Ruuskanen, C. Bajamundi, A. Kosonen, P. Simell, J. Ahola, C. Frilund, J. Elfving, M. Reinikainen, N. Heikkinen, J. Kauppinen, P. Piermartini, Power-to-X technology using renewable electricity and carbon dioxide from ambient air : SOLETAIR proof-of-concept and improved process concept, Journal of CO2 Utilization 28 (September) (2018) 235–246. doi:10.1016/j.jcou.2018.09.026.
URL https://doi.org/10.1016/j.jcou.2018.09.026

[4] M. S. Dresselhaus, I. L. Thomas, Alternative energy technologies, Nature 414 (2001) 332–337. doi:10.1038/35104599.

[5] N. Z. Muradov, T. N. Vezirog, Green path from fossil-based to hydrogen economy : An overview of carbon-neutral technologies 33 (2008) 6804–6839. doi:10.1016/j.ijhydene.2008.08.054.

[6] K. Zeng, D. Zhang, Recent progress in alkaline water electrolysis for hydrogen production and applications, Progress in Energy and Combustion Science 36 (3) (2010) 307–326. doi:10.1016/j.pecs.2009.11.002.
URL http://dx.doi.org/10.1016/j.pecs.2009.11.002

[7] S. Marini, P. Salvi, P. Nelli, R. Pesenti, M. Villa, M. Berrettoni, G. Zangari, Y. Kiros, Advanced alkaline water electrolysis, Electrochimica Acta 82 (2012) 384–391. doi:10.1016/j.electacta.2012.05.011.
URL http://dx.doi.org/10.1016/j.electacta.2012.05.011

[8] L. Carrette, K. A. Friedrich, U. Stimming, Fuel Cells - Fundamentals and Applications (1) (2001) 5–39. doi:https://doi.org/10.1002/1615-6854(200105)1:1¡5::AID-FUCE5¿3.0.CO;2-G.

21

[9] Y. Li, J. Lu, Metal - Air Batteries : Will They Be the Future Electrochemical Energy Storage Device of Choice? (2) (2017) 1370–1377. doi:10.1021/acsenergylett.7b00119.

[10] G. Kumar, R. G. Saratale, A. Kadier, P. Sivagurunathan, G. Zhen, S. H. Kim, G. D. Saratale, A review on bio-electrochemical systems (BESs) for the syngas and value added biochemicals production, Chemosphere 177 (2017) 84–92. doi:10.1016/j.chemosphere.2017.02.135.
URL http://dx.doi.org/10.1016/j.chemosphere.2017.02.135

[11] S. N. Nangle, K. K. Sakimoto, P. A. Silver, D. G. Nocera, Biological-inorganic hybrid systems as a generalized platform for chemical production, Current Opinion in Chemical Biology 41 (2017) 107–113. doi:10.1016/j.cbpa.2017.10.023.
URL http://dx.doi.org/10.1016/j.cbpa.2017.10.023

[12] S. Nian-Tzu, H. Sung-Fu, Q. Quan, Z. Nan, X. Yi-Jun, C. Hao Ming, Electrocatalysis for the oxygen evolution reaction : recent development and future perspectives, Chemical Society Reviews 46 (2017) 337–365. doi:10.1039/C6CS00328A.
URL http://dx.doi.org/10.1039/C6CS00328A

[13] M. Tahir, L. Pan, F. Idrees, X. Zhang, L. Wang, J. J. Zou, Z. L. Wang, Electrocatalytic oxygen evolution reaction for energy conversion and storage: A comprehensive review, Nano Energy 37 (February) (2017) 136–157. arXiv:/doi.org/10.1016/j.nanoen.2017.05.022, doi:10.1016/j.nanoen.2017.05.022.
URL http://dx.doi.org/10.1016/j.nanoen.2017.05.022

[14] Y. Cheng, S. Ping, Advances in electrocatalysts for oxygen evolution reaction of water electrolysis-from metal oxides to carbon nanotubes-doi:10.1016/j.pnsc.2015.11.008.

[15] A. Ursúa, L. Gandía, P. Sanchis, Hydrogen production from water electrolysis: Current status and future trends, Proceedings of the IEEE 100 (2) (2012) 410 –426. doi:10.1109/JPROC.2011.2156750.

[16] A. Irshad, N. Munichandraiah, High Catalytic Activity of Amorphous Ir-Pi for Oxygen Evolution Reaction, ACS Appl. Mater. Interfaces 7 (2015) 1576515776. doi:10.1021/acsami.5b02601.

[17] Q. Liu, Z. Chen, Z. Yan, Y. Wang, S. Wang, S. Wang, G. Sun, Crystal-plane-dependent activity of spinel Co3O4 towards water splitting and oxygen reduction reaction, ChemElectroChem 5 (2018) 1080–1086. doi:10.1002/celc.201701302.

[18] J. Zaffran, M. C. Toroker, A deep understanding of oxygen evolution reaction on two- dimensional NiO2 catalyst, ChemElectroChem 4 (2017) 2764–2770. doi:10.1002/celc.201700445.

[19] J. Huang, Y. Su, Y. Zhang, W. Wu, C. Wu, Y. Sun, Y. Li, X. Jie, FeOx/FeP Hybrid Nanorods Neutral Hydrogen Evolution Electrocatalysis: Insight into Interface, J. Mater. Chem. A 6 (2018) 9467–9472. doi:10.1039/C8TA02204F.

[20] C. G. Morales-guio, L. Liardet, X. Hu, Oxidatively Electrodeposited Thin-Film Transition Metal (Oxy)hydroxides as Oxygen Evolution Catalysts, J. Am. Chem. Soc. 138 (2016) 8946–8957. doi:10.1021/jacs.6b05196.

[21] X. Long, G. Li, Z. Wang, H. Zhu, T. Zhang, S. Xiao, W. Guo, S. Yang, X. Long, G. Li, Z. Wang, H. Zhu, T. Zhang, S. Xiao, W. Guo, Metallic Iron-Nickel Sulfide Ultrathin Nanosheets As a Highly Active Electrocatalyst for Hydrogen Evolution Reaction in Acidic Media Metallic Iron-Nickel Sulfide Ultrathin Nanosheets As a Highly Active Electrocatalyst for Hydrogen Evolution Reaction in Ac, J. Am. Chem. Soc. 137 (2015) 11900–11903. doi:10.1021/jacs.5b07728.

[22] Z. Ma, H. Meng, M. Wang, B. Tang, J. Li, Porous Ni-Mo-S Nanowire Network Film Electrode as High- efficiency Bifunctional Electrocatalyst for Overall Water Splitting, ChemElectroChem 5 (2017) 335–342. doi:10.1002/celc.201700965.

[23] X. Wang, W. Li, D. Xiong, D. Y. Petrovykh, L. Liu, Bifunctional Nickel Phosphide Nanocatalysts Supported on Carbon Fiber Paper for Highly Efficient and Stable Overall Water Splitting, Adv. Funct. Mater. 26 (2016) 4067–4077. doi:10.1002/adfm.201505509.

[24] K. Xu, P. Chen, X. Li, Y. Tong, H. Ding, X. Wu, K. Xu, P. Chen, X. Li, Y. Tong, H. Ding, X. Wu, W. Chu, Metallic Nickel Nitride Nanosheets

23

Realizing Enhanced Electrochemical Water Oxidation, J. Am. Chem. Soc. 137 (2015) 4119–4125. doi:10.1021/ja5119495.

[25] X. Chen, Z. Yu, L. Wei, Z. Zhou, S. Zhai, J. Chen, Ultrathin nickel boride nanosheets anchored on functionalized carbon nanotubes as bifunctional electrocatalysts for overall water splitting, J. Mater. Chem. A 7 (2019) 764–774. doi:10.1039/c8ta09130g.

[26] J. Masa, P. Weide, D. Peeters, I. Sinev, W. Xia, Z. Sun, C. Somsen, M. Muhler, W. Schuhmann, Amorphous Cobalt Boride (Co2B) as a Highly Efficient Nonprecious Catalyst for Electrochemical Water Splitting : Oxygen and Hydrogen Evolution, Adv. Energy Mater. 6 (2016) 1502313. doi:10.1002/aenm.201502313.

[27] L. Liao, S. Wang, J. Xiao, X. Bian, Y. Zhang, A nanoporous molybdenum carbide nanowire as an electrocatalyst for hydrogen evolution reaction, Energy Environ. Sci. 7 (2014) 387–392. doi:10.1039/c3ee42441c.

[28] H. Lin, Z. Shi, S. He, X. Yu, S. Wang, Q. Gao, Y. Tang, Heteronanowires of MoCMo2C as Efficient Electrocatalysts for Hydrogen Evolution Reaction, Chem. Sci. 7 (2016) 3399–3405. doi:10.1039/C6SC00077K.

[29] C. Tang, N. Cheng, Z. Pu, W. Xing, X. Sun, NiSe Nanowire Film Supported on Nickel Foam : An Efficient and Stable 3D Bifunctional Electrode for Full Water Splitting, Angew. Chem. Int. Ed. 54 (2015) 9351–9355. doi:10.1002/anie.201503407.

[30] J. Tian, Q. Liu, N. Cheng, A. M. Asiri, X. Sun, Self-Supported Cu3P Nanowire Arrays as an Integrated High-Performance Three-Dimensional Cathode for Generating Hydrogen from Water, Angew.Chem.Int. Ed. 53 (2014) 9577–9581. doi:10.1002/anie.201403842.

[31] J. Huang, Y. Li, Y. Xia, J. Zhu, Q. Yi, H. Wang, J. Xiong, Flexible cobalt phosphide network electrocatalyst for hydrogen evolution at all pH values 10 (2017) 1010–1020. doi:10.1007/s12274-016-1360-y.

[32] B. Zhang, Y. H. Lui, H. Ni, S. Hu, Bimetallic (FexNi1x)2P nanoarrays as exceptionally efficient electrocatalysts for oxygen evolution in alkaline and neutral media, Nano Energy 38 (April) (2017) 553–560. doi:10.1016/j.nanoen.2017.06.032.
URL http://dx.doi.org/10.1016/j.nanoen.2017.06.032

[33] B. Zhang, Y. H. Lui, L. Zhou, X. Tang, S. Hu, An alkaline electro-activated Fe-Ni phosphide nanoparticle-stack array for high-performance oxygen evolution under alkaline and neutral conditions, Journal of Materials Chemistry A 5 (26) (2017) 13329–13335. doi:10.1039/c7ta03163g.

[34] M. W. Kanan, D. G. Nocera, In Situ Formation of an Oxygen-Evolving Catalyst in Neutral Water Containing Phosphate and Co2+, Science 321 (2008) 1072–1075. doi:10.1126/science.1162018.

[35] Z. Wang, Z. Lin, P. Diao, Hybrids of iridiumcobalt phosphates as a highly efficient electrocatalyst for the oxygen evolution reaction in neutral solution, Chemical Communications 55 (2019) 3000–3003. doi:10.1039/C8CC10278C.
URL http://dx.doi.org/10.1039/C8CC10278C

[36] P. T. Babar, A. C. Lokhande, H. J. Shim, M. G. Gang, B. S. Pawar, S. M. Pawar, J. Hyeok, SILAR deposited iron phosphate as a bifunctional electrocatalyst for efficient water splitting, Journal of Colloid And Interface Science 534 (2018) 350–356. doi:10.1016/j.jcis.2018.09.015.
URL https://doi.org/10.1016/j.jcis.2018.09.015

[37] D. Zhong, L. Liu, D. Li, C. Wei, Q. Wang, G. Hao, Q. Zhao, J. Li, Facile and fast fabrication of iron-phosphate supported on nickel foam as a highly efficient and stable oxygen evolution catalyst, J. Mater. Chem. A 5 (2017) 18627–18633. doi:10.1039/C7TA05580C.

[38] Q. Zhang, T. Li, J. Liang, N. Wang, X. Kong, J. Wang, H. Qian, Y. Zhou, F. Liu, C. Wei, Y. Zhao, X. Zhang, High Wettable and Metallic NiFe-Phosphate/Phosphide Catalyst Synthesized by Plasma for High Efficient Oxygen Evolution Reaction, J. Mater. Chem. A 6 (2018) 7509–7516. doi:10.1039/C8TA01334A.

[39] J. Xing, H. Li, M. M.-c. Cheng, S. M. Geyer, K. Y. S. Ng, Electro-synthesis of 3D porous hierarchical Ni Fe phosphate film / Ni foam as a high-efficiency bifunctional electrocatalyst for overall water splitting, J. Mater. Chem. A 4 (2016) 13866–13873. doi:10.1039/c6ta05952j.

[40] Q. Liang, L. Zhong, C. Du, Y. Luo, Y. Zheng, S. Li, Achieving highly efficient electrocatalytic oxygen evolution with ultrathin 2D Fe-doped nickel thiophosphate nanosheets, Nano Energy 47 (2018) 257–265.

doi:10.1016/j.nanoen.2018.02.048.
URL https://doi.org/10.1016/j.nanoen.2018.02.048

[41] Y. Li, C. Zhao, Iron-Doped Nickel Phosphate as Synergistic Electrocatalyst for Water Oxidation, Chem. Mater 28 (2016) 56595666. doi:10.1021/acs.chemmater.6b01522.

[42] K. Jin, J. Park, J. Lee, K. D. Yang, G. K. Pradhan, S. H. Kim, S. Han, K. T. Nam, Hydrated Manganese(II) Phosphate (Mn3(PO4)2 · 3H2O) as a Water Oxidation Catalyst, J. Am. Chem. Soc. 136 (2014) 74357443. doi:https://doi.org/10.1021/ja5026529.

[43] R. Guo, X. Lai, J. Huang, X. Du, Y. Yan, Y. Sun, G. Zou, J. Xiong, Phosphate-based electrocatalysts for water splitting: a review on recent progress, ChemElectroChem 5 (2018) 3822–3834. doi:10.1002/celc.201800996.

[44] G. Givirovskiy, V. Ruuskanen, L. S. Ojala, M. Lienemann, P. Kokkonen, J. Ahola, Electrode material studies and cell voltage characteristics of the in situ water electrolysis performed in a pH-neutral electrolyte in bioelectrochemical systems, Heliyon 5 (2019) e01690. doi:10.1016/j.heliyon.2019.e01690.
URL https://doi.org/10.1016/j.heliyon.2019.e01690

[45] G. Givirovskiy, V. Ruuskanen, L. S. Ojala, P. Kokkonen, J. Ahola, In Situ Water Electrolyzer Stack for an Electrobioreactor, Energies 12 (1904) (2019) 1–13. doi:10.3390/en12101904.

[46] T. Reier, M. Oezaslan, P. Strasser, Electrocatalytic Oxygen Evolution Reaction (OER) on Ru , Ir , and Pt Catalysts : A Comparative Study of Nanoparticles and Bulk Materials, ACS Catalysis 2 (2012) 17651772. doi:https://doi.org/10.1021/cs3003098.

[47] J. O. Bockris, Kinetics of activation controlled consecutive electrochemical reactions: Anodic evolution of oxygen, The Journal of Chemical Physics 24 (4) (1956) 817–827. doi:10.1063/1.1742616.